npj | flexible electronics

Article

Published in partnership with Nanjing Tech University

https://doi.org/10.1038/s41528-024-00340-0

# Conformal printed electronics on flexible substrates and inflatable catheters using lathe-based aerosol jet printing



Hansel Alex Hobbie[1], James L. Doherty[1], Brittany N. Smith[1], Paolo Maccarini[1,2] & Aaron D. Franklin[1,3]

With the growth of additive manufacturing (AM), there has been increasing demand for fabricating conformal electronics that directly integrate with larger components to enable unique functionality. However, fabrication of conformal electronics is challenging because devices must merge with host substrates regardless of curvilinearity, topography, or substrate material. In this work, we employ aerosol jet (AJ) printing, an AM method for jet printing electronics using ink-based materials, and a custom-made lathe mechanism for mounting flexible substrates and 3D objects on a rotating axis. Using this method of lathe-based AJ printing, conformal electronics are printed around the circumference of rotational bodies with 3D curvilinear surfaces through cylindrical-coordinate motion. We characterize the diverse capabilities of lathe AJ (LAJ) printing and demonstrate flexible conformal electronics including multilayer carbon nanotube transistors. Lastly, a graphene sensor is conformally printed on an inflated catheter balloon for temperature and inflation monitoring, thus highlighting the versatilities of LAJ printing.

Additive manufacturing (AM) of electronics is a promising approach for pursuing new application spaces with cost-effective, readily customizable devices that would not be well-suited to conventional fabrication[1–3]. Conventional fabrication methods require rigid planar substrates and restrictive processing steps (e.g., high temperatures, vacuum conditions), which hinder application formats beyond that of chips and boards[4,5]. Alternatively, AM methods can move beyond planar structures and restrictive processing techniques to achieve three-dimensional (3D) fabrication of electronic devices[6,7] with demonstrated applicability to flexible/stretchable electronics[8–10], organic electronics[11–13], and conformal electronics[14,15], which refers to devices that are built to situate flush with their host substrate (regardless of rigid 3D topography or dynamic movement).

Conformal electronics address a distinct need for electronic functionality being integrated onto diverse flexible surfaces, yielding notable advancements in on-skin/wearable technologies[16–19], embedded componentry for aerospace[20], and Internet of Things devices[21–23]. While the applications of conformal electronics are numerous, the manufacturing techniques for building such devices are limited. Methods for realizing conformal electronics fall into two major categories: (1) soft lithography followed by transfer/stamping[24–27] and (2) direct-write (DW) printing[28–31]. Soft-lithography techniques use conventional fabrication to produce electronic devices on flexible substrates; these techniques are well established but also complex, expensive, and restrictive, as mentioned earlier. Then, by a soft transfer or stamping process, the fabricated devices are wrapped conformally onto a target component. Although effective for some applications, this transfer approach lacks the versatility of AM and faces obstacles in scaling up production. On the other hand, DW printing methods are inherently 3D and embody the principles of AM technology in providing a simple, cost-effective, and adaptable fabrication process that is truly additive in nature[28].

A distinct advantage of DW printing approaches for conformal electronics is their non-contact deposition of conformal microstructures using a broad catalog of printable materials[28]. Within DW printing methods, droplet-based approaches such as aerosol jet (AJ) printing[32–34] and inkjet printing[35–37] have substantial value for their ability to deposit virtually any material that can be suspended in a colloidal ink solution. While conformal devices have been demonstrated using inkjet printing[38,39], AJ printing offers improvements of specific benefit to conformal electronics fabrication based on its large standoff distance (3–5 mm above the target substrate) and versatile methods for aerosolized deposition[40–42] (see Supplementary Fig. 1). Due to the jetting nature of AJ printing, changes in distance or angle between the print nozzle and target substrate have reduced effect on the thickness and width of printed traces until reaching overly oblique deposition (>135°) and large standoff distances (>5 mm)[43]. These unique qualities enable conformal AJ printing onto complex structures with a range of surface conditions (e.g., material

[1]Department of Electrical and Computer Engineering, Duke University, Durham, NC, USA. [2]Department of Anesthesiology, Duke University, Durham, NC, USA. [3]Department of Chemistry, Duke University, Durham, NC, USA. e-mail: aaron.franklin@duke.edu

roughness or topography) because the jetted material can be deposited onto surfaces from a distance[44–47].

Although AJ printing is ideal for achieving conformal printing, there are limitations when a substrate possesses curvilinear features that are steep enough to make the angle of deposition from the print nozzle far off orthogonal, thus severely impacting print quality. To achieve conformal printing for curvilinear substrates a more sophisticated motion system is required that can adequately move and position the substrate at an orthogonal angle of print incidence. There exist advanced motion systems like 5-axis trunnion-based printers that utilize two rotational axes in addition to 3D linear motion to fix the orientation of the substrate and nozzle at an orthogonal print incidence regardless of substrate curvilinearity[48,49]. The drawback of these systems is the machine complexity needed to achieve complete 5-axis control, which can prohibitively raise cost when scaling up to commercial-level manufacturing. A less complex alternative for conformal printing onto curvilinear surfaces is to use a motion system with one axis of rotation. With rotation around just one axis, it is possible to move a nozzle circumferentially around radial curvature, which is ideal for conformity around curved 3D shapes like cylinders. One-axis rotation does not fully solve the problem of conformity onto multidirectional curvature (e.g., spherical surfaces); however, there are a number of conformal applications that can be unlocked just by utilizing a motion system with cylindrical-coordinate capabilities.

There are specific application needs for conformal electronics on 3D rotational bodies that would benefit from a simple yet versatile AM technique. For example, catheters and inflatable catheter balloons, which are inherently cylindrical and rotatable around a single axis, are used in surgical procedures throughout the body such as endoscopy [50], angioplasty [51], and elution-based drug delivery [52]. The cylindrical 3D body and soft-material surface of these catheters make it difficult to directly add conformal electronics, with a few demonstrations of conformally adding functionality for tactile detection[53], temperature sensing[54], and ablative procedures[55,56]. The methods used to realize these limited demonstrations were all related to soft lithography with a transfer process that placed electronics onto the catheters[57–60]. However, these techniques require a secondary substrate to be used with the catheter, can only provide semicircular conformity, and require multi-step conventional processing. Alternatively, AJ printing shows great potential for conformal DW fabrication of electronics on catheters. In works by Jordan et al. and Will et al., AJ printing was used to fabricate resonant circuits on the surface of catheters to provide low-profile tracking of the catheter during MRI procedures[61,62]. Although the authors demonstrated functional conformal devices on catheters, they both used strictly cartesian movement systems that limited their fabrication to a process requiring multiple printing steps and manual interaction to correctly fix the substrate under the nozzle. By utilizing a cylindrical-coordinate motion system with rotational control, the limitations of cartesian AJ printing could be overcome and conformal DW printing onto catheters would become trivial such that full designs could be patterned in a single print step.

In this work, we developed a custom solution to achieve conformal AJ printing onto flexible curvilinear surfaces and 3D rotational substrates that utilizes lathe-based cylindrical-coordinate motion to rotate a substrate fixed on an axis. Evidence of the effect of print incidence on conformal printing applications is presented, along with a thorough exploration of the lathe AJ printing (LAJ) technology—coined for its similarity to the function of an axially rotating lathe. This printing technique allows for cartesian motion to be translated into 3D cylindrical rotation, which is ideal for conformity on 3D curvature. The mechanisms of operation are presented along with a full characterization of mechanical performance down to the micron scale. The capabilities of the LAJ printing method are highlighted by demonstrating multiple applications of the technology with relevancy to flexible and sustainable electronics, complex-geometry conformal printing, as well as catheter-based electronic devices. In the final demonstration, we demonstrate DW printing of flexible electronics onto inflatable catheter ballons, which could simplify the integration of electronics in the many medical procedures involving catheters and catheter balloons. Notably, we demonstrate that our system is applicable for any catheter with substrate dimensions under 40 mm in diameter, emphasizing that LAJ printing can be employed for conformal on catheter electronics with many possible applications.

## Results and discussion

### Lathe printer attachment conceptualization and design

To achieve cylindrical-coordinate-based control of printing, a custom attachment for the $x$–$y$ platen of a commercial AJ printer (Optomec AJ300) was developed, as shown in Fig. 1. In the computer aided design (CAD) diagram of the lathe mechanism, the various features that provide the lathe functionality can be readily identified. The primary feature worth noting is the mechanism for translating linear motion in the cartesian $x$-axis to rotational motion in the cylindrical $\theta$-axis while maintaining linear motion in the axial direction along the $y$/$z$-axis. This translation is achieved by the rack, pinion, and axle clamp, which serve as the junction between the printer-controlled platen and the suspended rotating axle. The pinion is affixed on an axis above the rack by a linear motion shaft with screw-tapped ends that allow for on-axis attachments like the pinion and axle clamp. The pinion interlocked with the platen-fixed rack provides the rotation to the suspended axle, and the axle clamp, which locks onto a ball bearing in a guide rail, providing the linear motion to the shaft regardless of position on the $x$-axis (see Fig. 1a). This shaft is suspended above the rack by a position-adjustable support with two ball bearings to allow smooth rotation. This support is attached to the printer body separately from the platen and has adjustable guides to set the rotating axle directly under the nozzle tip. Depending on the direction of the platen movement, the suspended axle can freely rotate within the bearings, slide through the bearings to allow linear axial motion, or both simultaneously. The length of the shaft determines the range of axial motion, and full circumferential rotation enables deposition onto substrates of any diameter <40 mm, which is the largest substrate-holding mandrel that can be fit under the nozzle (see Supplementary Fig. 2). The significant advantage of utilizing a platen-mounted rack to translate linear motion to axial rotation is that this is a readily scalable solution, such that multiple suspended axles can be supported by the system without the addition of any motors or components beyond the additional substrate-supporting mandrels.

Using this mechanism, cylindrical-coordinate LAJ printing is achieved, making it possible to conformally print around the entire circumference of rotationally symmetric bodies without manual interaction. Examples of substrates that this configuration can conformally print onto include flexible films wrapped around cylinders, 3D rotational solids (cylinders, cones, helices, etc.), and hollow rotational solids such as tubing or balloons. Cylindrical bodies are the ideal case for this system, as the print incidence will be perfectly normal for the entire curved surface. However, with the mechanism it is possible to conformally print around 360° of rotation for any solid with a definable axis, which supports a high degree of applicability to any number of substrate geometries.

### Significance of the angle of print incidence in conformal printing

The angle of print incidence for AJ printing is defined here as the angle between the target substrate and the aerosol stream that is responsible for material deposition onto the substrate. In the ideal printing scenario, the angle of incidence is always kept at 90° such that the deposition is normal to the substrate and factors affecting thin-film formation (e.g., surface hydrophobicity, inclination) are limited[63–65]. Maintaining normal incidence during deposition is important because at increasing degrees of hydrophobicity, a droplet has less surface adhesion and will roll across a surface more easily at oblique angles of incidence. Through the practice of treating surfaces to lower hydrophobicity and keeping the print nozzle orthogonal over the substrate, print adhesion improves greatly for a variety of substrates. In planar AJ printing onto a flat substrate, it is trivial to maintain normal incidence; however, for conformal printing applications where the

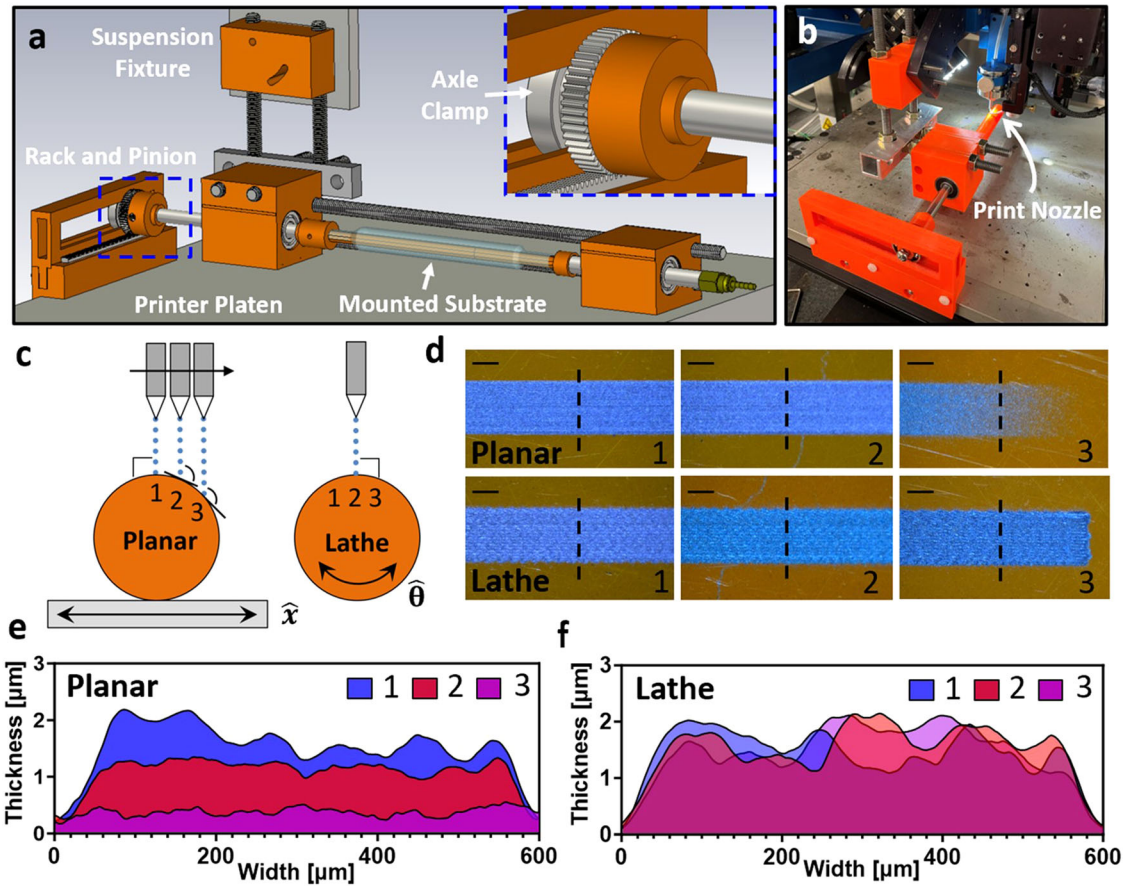


**Fig. 1 | Lathe aerosol jet (LAJ) printing mechanism and the impact of angle of print incidence on conformal films. a** CAD diagram of LAJ printer attachment and closeup image of the rack and pinion with axle clamp. **b** Picture of LAJ printer attachment secured to the printing system with deposition nozzle located above cylindrical rotating mandrel. **c** Illustration of the angle of print incidence for planar (stage linear motion in $x$) and lathe (substrate rotational motion in $\theta$) AJ printing. **d** Images of planar and LAJ printed graphene traces at positions 1, 2, and 3 separated by ~5.9 mm for each method (dashed line indicates cross-section location with scale bar of 250 μm). **e** Thickness profiles across the width of planar AJ printed graphene traces at positions 1, 2, and 3—note the significant drop in thickness at position 3 where the incident angle was ~75°. **f** Thickness profiles across the width of LAJ printed graphene traces at positions 1, 2, and 3 showing consistency of thickness distribution at each site.

substrate topography presents varying degrees of nonplanarity, the ideal normal incidence is almost entirely lost with planar AJ printing. While the loss of normal incidence does not strictly mean an inability to print conformally, it does establish a discrepancy from the assumed ideal case that will create issues in print uniformity and design at increasingly steep angles of incidence. An example of this issue is presented in Fig. 1c–f, wherein planar and LAJ conformal printing of graphene ink onto a polyimide sheet wrapped about a cylindrical body is compared. The illustration in Fig. 1c shows that for planar AJ printing, the angle of print incidence is only normal at the acme of the cylinder (position 1) and continues to increase as the cylinder slopes away from the $x$-axis (positions 2 and 3). In contrast, LAJ printing maintains normal print incidence around the entire circumference of the cylinder because of the $\theta$-axis rotation of the substrate, which holds the three positions as the acme of the cylinder directly under the nozzle throughout printing. It should be noted that in this experiment, the standoff distance for the planar case is also increasing with angle of incidence because the nozzle is not actively moving in the $z$-axis to correct for the change in distance above the substrate. However, even with active $z$-axis control the angle of incidence will be non-orthogonal and achieving adequate conformity around a circumference remains a major challenge.

The significance of the difference between planar and LAJ printing on a curved surface becomes visually clear in Fig. 1d when looking at the quality of printed traces between the two print methods at positions 1, 2, and 3 (each ~5.9 mm apart). At positions 1 and 2, the planar and lathe approaches produce visually consistent traces because of the near-normal incidence in the planar case. At position 3, however, when the angle of incidence is steepest (>160°) for the planar approach, the printed trace becomes thin and patchy in comparison to the lathe printed trace, which maintains a uniform appearance consistent with positions 1 and 2. Cross-sectional thickness profiles of these printed traces at the corresponding positions are shown in Fig. 1e, f for the planar and lathe approaches, respectively. The planar traces exhibit nonuniformity in thickness between the three positions, whereas the conformal traces produced by LAJ printing are effectively the same thickness regardless of position thanks to rotation of the substrate keeping the incident angle fixed. From this demonstration, it is shown that for successful conformal printing onto 3D curved substrates it is critical to use a system with rotational movement because a planar cartesian motion system cannot provide normal print incidence for curved features of any kind.

### Translation of motion and the importance of the diametric ratio

The ratio between the substrate diameter ($D_S$) and the pinion diameter ($D_P$), referred to as the diametric ratio ($D_S/D_P$) is of critical design importance because it can amplify or diminish the actual motion and print speed for the substrate under the nozzle. If the two diameters are equal, the $x$- and $y$-direction movement of the printer platen is translated at a 1:1 ratio with the $\theta$- and $z$-direction movement of the rotating substrate. However, if the diameters are unequal then the translation of the $x$-direction platen movement to the $\theta$-direction mandrel rotation will be multiplied by the diametric ratio, as illustrated in Supplementary Fig. 3. As a result, the true displacement ($d$) and print speed ($v$) of the rotating substrate in the $\theta$- and $z$-

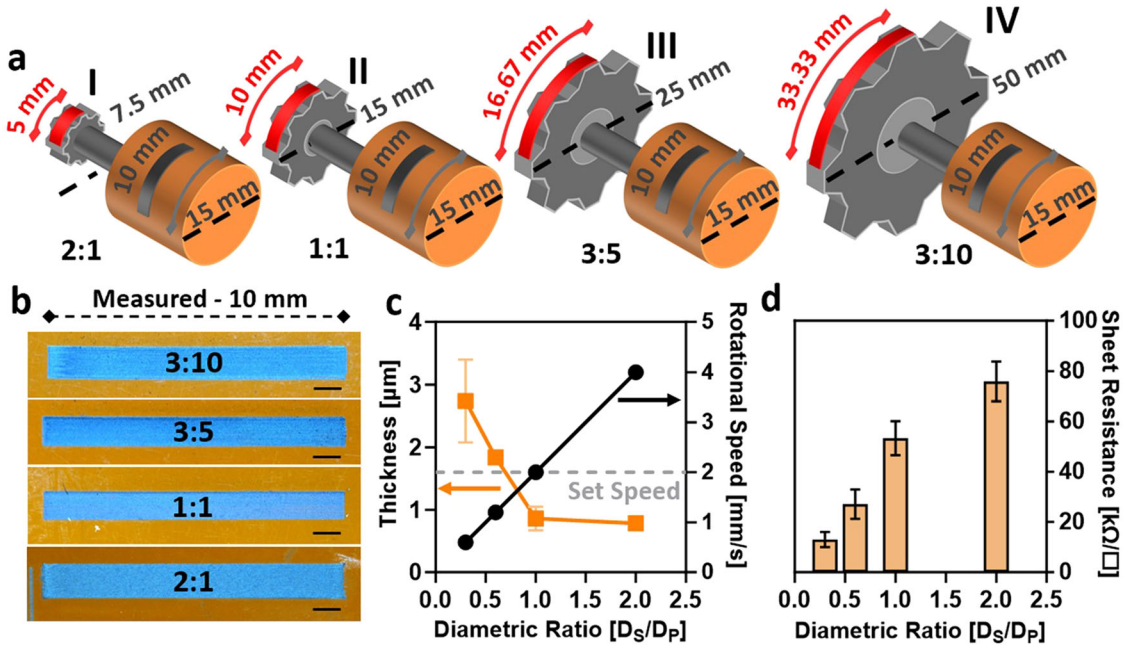


**Fig. 2 | Characterization of lathe system translation of motion. a** Illustration of the ratio-adjusted design of lathe aerosol jet (LAJ) printed graphene traces for the four diametric ratios studied. **b** Microscope images of LAJ printed graphene traces using different diametric ratios, scale bar is 1 mm. **c** Thickness of graphene traces and rotational print speed for different diametric ratios with error bars indicating standard deviation using $n = 3$ samples for each ratio. **d** Plot of sheet resistance for graphene traces printed using different diametric ratios with error bars indicating standard deviation using $n = 3$ samples for each ratio.

directions will differ from the movement and print speed of the planar platen according to the four equations provided in the Supplementary Information.

Although it is ideal to match the diameters of the pinion and a given substrate, it is much easier to acknowledge the difference in the two diameters, as mapped out in Supplementary Fig. 4. For the work presented here, four pinions were tested with diameters of 7.5, 15, 25, and 50 mm, and a 15 mm cylindrical mandrel (Supplementary Fig. 5) to vary the diametric ratio as illustrated in Fig. 2a. Due to the effect of the diametric ratio, it is important to adjust the design file by either elongating or shortening dimensions in the $\theta$-direction to achieve the desired pattern. In Fig. 2b, the as-printed traces for each of the diametric ratios were imaged, and each trace is shown to be 10 mm in length as intended, despite the diametric ratio affecting the design dimensions. Since the diametric ratio will also have an effect on the rotational speed, it is important to consider how the true rotational speed of the substrate will impact printing. For the graphene traces, a linear print speed of 2 mm/s was set for the motorized platen, and the actual print speed of the rotating mandrel was determined according to the diametric ratio, as plotted in Fig. 2c for the four example cases. In this plot, the thickness of the printed traces is also provided relative to the true print speed. As would be expected, for faster print speeds at higher diametric ratios the printed traces become thinner than when they are printed at lower diametric ratios with slower print speeds. Consequently, for the thicker traces printed with the lowest diametric ratios there is substantially less sheet resistance than for the relatively thinner traces produced at higher ratio values, as shown in Fig. 2d. This trend in sheet resistance is also expected, as the thicker traces contain a higher density of conductive material and thus exhibit lower sheet resistance than the thinner traces with less material. These results (Fig. 2) highlight the importance of understanding and characterizing the effect of the diametric ratio on LAJ printing so that appropriate design choices can be made.

## Characterizing performance of lathe mechanism

Considering the custom nature of this lathe mechanism prototype, it was critical to determine the accuracy of movement that is provided by the translation to cylindrical-coordinate motion. To measure the accuracy achieved by the lathe system, graphene traces were printed with center-to-center pitch from 500 μm down to 20 μm in both the circumferential ($\hat{\theta}$) and axial ($\hat{z}$) directions with a 1:1 diametric ratio (Supplementary Fig. 6). From the observed precision between the designed and measured pitch between lines, as shown in Fig. 3, the lathe mechanism was demonstrated to have controllable and accurate movement down to 20 μm in the circumferential and axial directions. Both the achieved resolution and uniformity of the lathe printing process on a cylindrical substrate are equal to the capabilities of planar printing onto flat surfaces because parity is provided by the rack and pinion motion translation mechanism. Additionally, to show the circumferential and axial directions can also be accurately moved simultaneously, traces were printed with center-to-center pitches of 500 μm down to 50 μm in ±45° angles relative to the axial direction with a 1:1 ratio (see Supplementary Fig. 7). Lastly, to verify that the lathe system accuracy is highly repeatable and maintained throughout printing, an experiment was devised in which the word "Duke" was printed three times in rapid succession with a 1:1 ratio and overlaid in the same location each time for print speeds of 2, 4, 6, 8, and 10 mm/s. The resulting prints are shown in Supplementary Fig. 8 with videos of the lathe mechanism operating at print speeds 4–10 mm/s provided in Supplementary Movie 1. The distinct lack of shifting and the clearly legible "Duke" for each of the print speeds is indicative of the accuracy and repeatability of the lathe mechanism across multilayer and variable-speed printing.

## Conformal and flexible electronic devices using LAJ printing

To demonstrate conformal and flexible electronics fabricated with LAJ printing, electronic devices of resistive traces, capacitors, and thin-film transistors (TFTs) were printed onto flexible substrates wrapped around cylindrical mandrels with a 1:1 diametric ratio. First, it was discovered that the resistance of infilled traces of printed graphene is dependent on the arc length (defined by the central angle and radius of the arc) and the infill direction, with axial infill yielding higher resistance at longer arc lengths, as seen in Fig. 4a. Resistance was measured in a two-terminal fashion by positioning micromanipulator probes at the ends of the long side of a trace. The two infill directions were tested

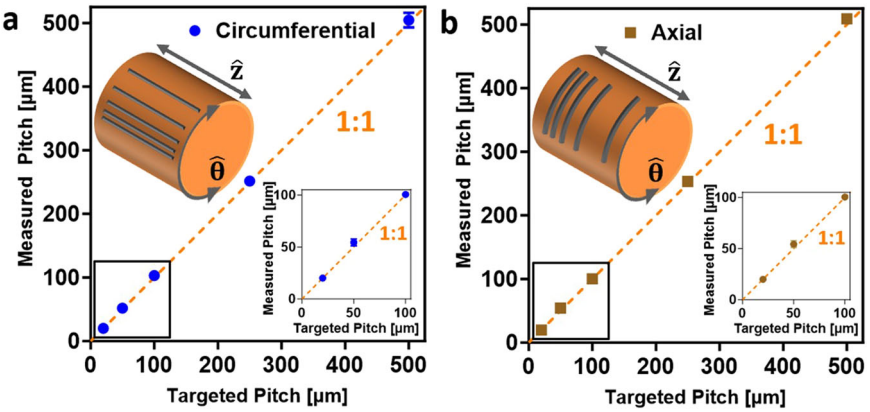


**Fig. 3 | Determining the resolution of the lathe system motion.** Plotted comparison of targeted pitch to the actual measured pitch for the **a** circumferential and **b** axial directions with error bars indicating standard deviation using $n = 4$ samples for each data point and the dashed line representing a 1:1 relation between the targeted and measured pitch (insets are magnified plots of the smallest pitches).

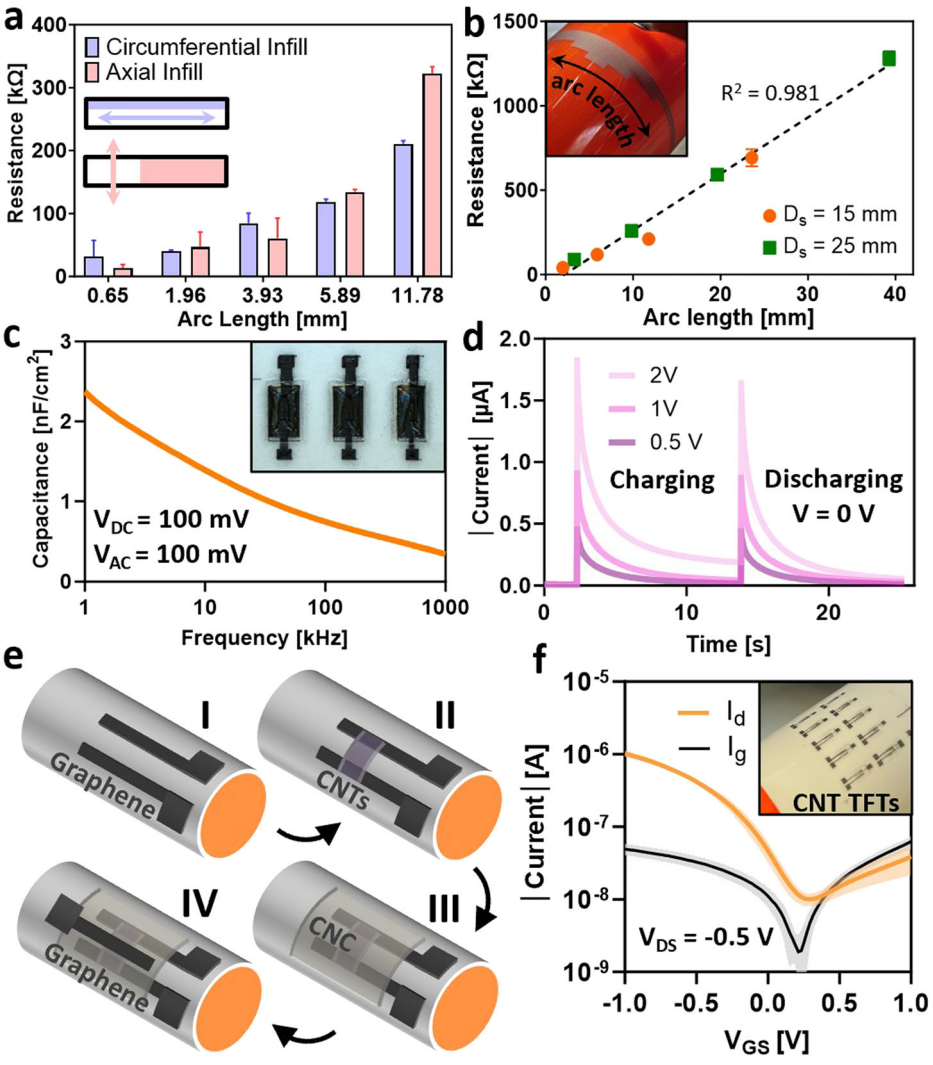


**Fig. 4 | Lathe aerosol jet printed graphene and CNT-TFTs. a** Resistance comparison between multiple arc lengths of graphene traces using different infill directions with error bars indicating standard deviation using $n = 3$ samples for each data point. **b** Resistance comparison between graphene traces printed on substrate-wrapped mandrels of different diameters and arc lengths. **c** Normalized capacitance across frequency for graphene/CNC capacitors. **d** Charging and discharging curves for graphene/CNC capacitors. **e** Fabrication process flow for LAJ printed CNT-TFTs on paper substrates on a 25 mm mandrel. **f** Device subthreshold characteristics of CNT-TFTs (inset is picture of devices with channel length and width of 225 and 200 µm, respectively). Data for both curves represent the average (solid line) ± the standard deviation (shaded region) for seven devices.

by printing graphene traces along the circumference of a substrate-wrapped 15 mm diameter mandrel with different central angles of 5°, 15°, 45°, and 90° defining the arc lengths. These traces exhibited mostly similar values of resistance up to an arc length of 11.78 mm (central angle of 90°), where the resistance of the arc trace began to deviate from previous values. This deviation is due to the axial-infilled trace being printed perpendicular to the arc length direction, which uses more individual microstrip lines to form a given trace. In contrast, the circumferential-infilled trace used longer printed lines with increasing arc length, but the number of lines used to form the trace remained the same. Thus, the circumferential-infilled traces maintained a linear resistance across increasing arc lengths while the axial-infilled traces showed a jump to higher resistance for long arc lengths because it was composed of more individual lines than the circumferential infill. Therefore, the infill patterns for the materials throughout this work were chosen in accordance with having the fewest individual lines

being printed for each geometry on a device layer to ensure consistent resistance.

In Fig. 4b, resistive traces of varying arc length were printed along the circumferences of 15- and 25-mm diameter mandrels using a diametric ratio of 1:1 and circumferential infill. Regardless of substrate diameter between the two mandrels, the resistance of the traces showed an expected trend of increasing resistance with arc length. These graphene traces were then measured by the four-point probe method and a relatively consistent range of sheet resistance values was observed across increasing arc length between the two mandrels (Supplementary Fig. 9). These results indicate the reliable performance of LAJ printing along increasing circumferential dimensions while also showing scalable application to substrates with different diameters.

While successful single-layer LAJ printing of electronic materials was critical to establish, the ability to fabricate multilayer electronics is more difficult and relies on accurate patterning and positioning between layers to achieve correct functionality. Given that AJ printing has shown great potential for producing eco-friendly and sustainable devices such as all-carbon recyclable electronics[66], cellulose nanocrystal (CNC), a carbonaceous ionic dielectric material, was chosen for use in the presented multilayer electronics as an insulating layer. To demonstrate a three-layered carbon-based device, a two-plate capacitor of graphene contacts and CNC was fabricated on a paper substrate wrapped around a 15 mm diameter mandrel using LAJ printing at a 1:1 ratio (Fig. 4c, d). The normalized capacitance across frequency for the capacitors of 0.81 $mm^2$ overlapping plate area decreases in a nonlinear fashion in accordance with the ionic nature of the CNC dielectric[67,68]. Furthermore, under applied voltages of 0.5, 1, and 2 V, exponential behavior of the capacitor charging and discharging currents is observed with measured leakage current for the 2 V case that diminishes for the lower voltages. These results demonstrate that simple multilayer electronic devices are readily fabricable with LAJ printing.

By expanding to four layers and using a top-gate transistor design that includes printed carbon nanotubes (CNTs) as the semiconducting layer, TFTs were fully LAJ printed on paper in accordance with the process flow illustrated in Fig. 4e. Briefly, source and drain contacts of graphene along with fiducial marks were printed onto a paper substrate mounted on a 25 mm diameter cylindrical mandrel. Then, the CNT channel was printed to bridge the two contacts followed by the CNC gate dielectric and a graphene top gate, all of which utilize the fiducial marks for correct alignment between the four TFT layers. It is worth noting that the toluene-based CNT ink used for these devices could pose some compatibility issues for substrates that display susceptibility to the toluene content, in which case, an alternative water-only CNT ink should be used to avoid any negative interactions between ink and substrate[69]. The switching characteristics of these TFTs are shown in Fig. 4f, wherein the drain current ($I_D$) and gate current ($I_g$) were measured for applied gate voltages ($V_{GS}$) from −1 to 1 V with a constant drain to source voltage ($V_{DS}$) of −0.5 V. The measured CNT-TFT devices possess repeatable and consistent switching behavior with an on/off-current ratio of ~$10^2$ and a full sweep range of only 2 V due to the ionic nature of the CNC gate dielectric drastically lowering the threshold voltage requirements. These devices have similarly low threshold voltage requirements ($V_T < 1$ V) and comparable device current ratios ($I_{ON}/I_{OFF}$: $10^2$–$10^3$) to previous examples of all-carbon printed TFT devices on paper despite the presented devices having no added ions or treatment to the wrapping polymer in the CNT channel[66]. However, these devices also suffer from a relatively high level of gate leakage current ($I_g > 1$ nA) that is a notable problem of devices with ionic dielectrics. The successful printing of these three-terminal, multilayer devices further corroborate the versatility and accuracy of LAJ printing across multiple layers and for different materials and substrates. LAJ printing is demonstrably capable of fabricating electronic devices onto nonplanar surfaces for conformal and flexible electronic applications alike.

### Conformal printing onto complex shapes with LAJ printing

From the demonstrations already presented, it is clear that LAJ printing achieves ideal orthogonal print incidence for conforming onto cylindrical bodies and flexible substrates bent around a convex radius. Coincidentally, without any modification to the actual lathe mechanism, the LAJ printing system also allows the print nozzle to be positioned at the focal point of concave curvature, as shown in Fig. 5a for a 15 mm diameter hollow half cylinder. In Fig. 5b, c, example patterns of graphene were deposited onto the concave mandrel with and without a fixed substrate to show that this setup can also be used to print onto flexible substrates bent into a compressive state at a concave angle.

Despite offering a simple and efficient method for conformal printing onto cylindrical curvature, the lathe-based approach still has limitations when working with multidirectional curves like spherical surfaces and nonuniform 2D curvatures. For complex geometries like these, the current maneuvering capabilities of the lathe prototype cannot achieve the ideal normal print incidence of 90°, and it may be better to consider systems with advanced functionality like the 5-axis printer. However, because of the standoff distance and jet-stream deposition of AJ printing, getting approximate uniformity in a printed trace is still possible for moderate angles of non-normal incidence. This tolerance of moderately non-normal incidence in conformal applications is demonstrated for LAJ printing in Fig. 5d, e by printing silver nanowires (AgNWs) onto a 3D-printed conical mandrel with a taper angle of 15°, resulting in a non-normal print incidence of 105° across the cone. For different substrates (e.g., cylindrical, conical, flat), the effects of printing with non-normal (oblique) incidence are identical and determined by the angle of print incidence from the nozzle position relative to the substrate[43]. In situations where the angle of incidence becomes increasingly oblique, like the example in Fig. 1 of printing onto a cylinder using planar movement, it was observed that thickness and uniformity of the printed films will quantifiably reduce. Oblique incidence will similarly impact cylindrical printing onto conical substrates, resulting in negligible effect for small taper angles but forming thinner and less defined printed traces for large tapers with extreme obliquity. As a further example of the adaptability of conformal AJ printing for small angles of obliquity, a 1000 µL pipette tip with a gradual taper of 7.5° was used as the substrate for a conformal graphene helix, which was printed spiraling down the length of the pipette tip from its narrow end as imaged in Fig. 5f, g. These examples serve to represent the tolerance of LAJ printing to gradual multidirectional curvature with its simple motion, however, there will still be limitations to the conformal complexity that can be realized without adding further axes of control.

### Catheter balloon functionalized with on-surface LAJ printed graphene sensor

Successfully fabricating conformal electronics onto 3D curvilinear substrates like cylinders is a non-trivial challenge that LAJ printing is well-suited to solve in a simple and readily scalable fashion. However, AM of conformal electronics becomes increasingly difficult for substrates like catheters and catheter balloons, which possess soft polymeric surfaces and non-rigid inflatable bodies that add complication to the print process. Although difficult to achieve, conformal fabrication of electronics directly onto catheter substrates is an important step in advancing catheter device technology for use in critical medical applications ranging from cancerous tissue ablation[56,58] to implanting long-term devices within the body[70,71]. During these crucial medical procedures catheters are integral, yet knowledge of conditions around the catheter such as temperature, contact/degree of inflation, and external pressure are practically unknown without built-in electronic functionality.

To enable the fabrication of conformal electronics onto catheters and catheter balloons, LAJ printing was modified to include a system for on-axis inflation that permits hollow and inflatable rotational bodies to be mounted on the lathe mechanism, as portrayed in Fig. 6a. Since the on-axis inflation required no other modification to the lathe mechanism beyond the inclusion of a rotating air inlet, the system capabilities for printing onto any substrate <40 mm in diameter hold true, even for inflated catheters. In Fig. 6b, examples of six commercially available catheter balloons are plotted according to the possible balloon diameters for the product and their

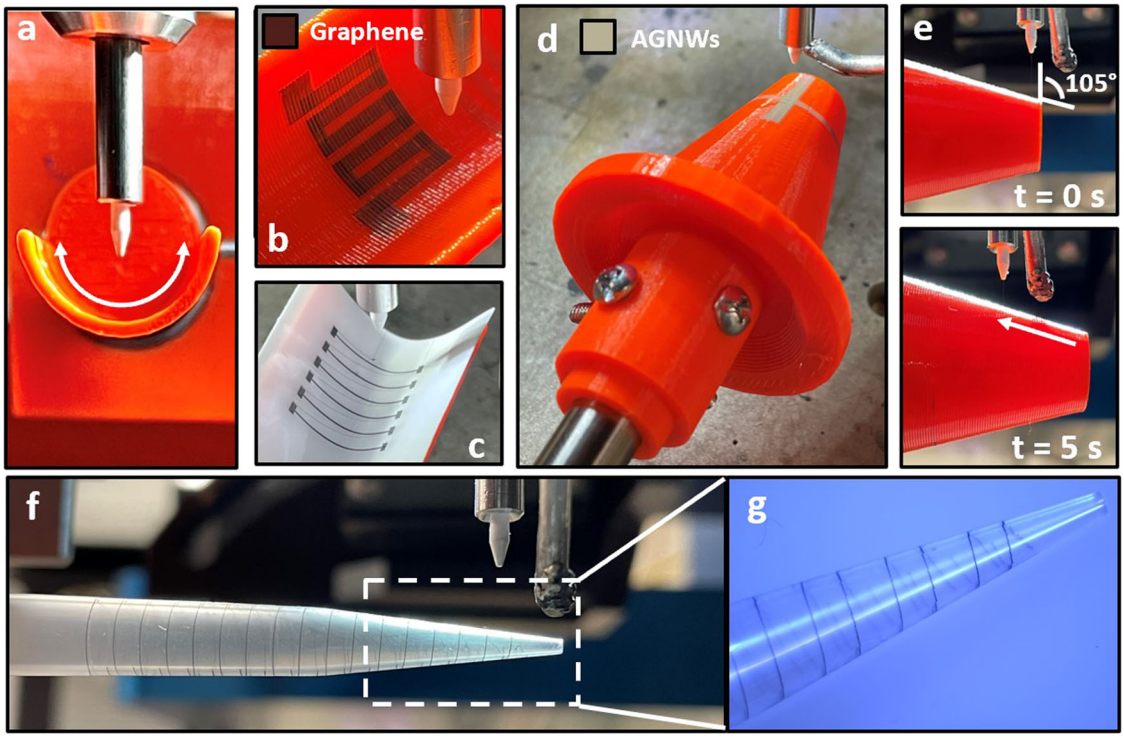


**Fig. 5 | Lathe aerosol jet printing onto complex substrates. a** Picture of AJ print nozzle fixed at the focal point above a concave mandrel. Pictures of printed graphene in **b** a meander line onto concave mandrel and **c** parallel lines on concavely bent paper substrate. **d** Picture of conical mandrel with printed AgNW traces. **e** Pictures of LAJ printing along the length of conical mandrel showing movement up the length of the cone after 5 s of printing. Pictures of **f** printing a graphene helix on 1000 µL pipette tip and **g** a magnified view of graphene helix on the pipette tip.

medical application space[72–77]. Also indicated in this plot is the 14 mm diameter thermoplastic polyurethane (TPU) catheter balloon used in this work, as shown in Fig. 6c, which is sized to be used for endoscopic applications[78]. These catheter dimensions compared to the compatible range of the lathe system make evident that the lathe mechanism presented in this work can be utilized for essentially any sized catheter regardless of medical application.

The six-step fabrication process flow for LAJ printing onto the inflated catheter balloon is detailed in Fig. 6d. The first pretreatment step is critical for cleaning the balloon substrate and improving the surface adhesion properties of the polymeric material to ensure good print quality. Then, after mounting the catheter and printing graphene traces onto it, an encapsulating layer of polydimethylsiloxane (PDMS/silicone) is dripped over the printed material for a few reasons: to ensure printed films do not delaminate from the surface during inflation/deflation, to provide a biocompatible coating over the chosen printed material, and also to reduce noise for printed sensors.

Using this fabrication process, a graphene meander line sensor was printed directly onto the surface of the inflated 14 mm TPU catheter balloon, as shown in Fig. 6e and Supplementary Movie 2. Graphene was selected for this sensor demonstration because of the environmentally sensitive material properties it offers, which cause a resistive change in the printed graphene based on temperature, stress/strain, and humidity[79]. Given that the graphene sensor is encapsulated by PDMS, humidity sensitivity is removed from the sensor leaving behind sensitivities to temperature and stress/strain. To demonstrate the value of having a functionalized catheter, the normalized resistive change of the graphene sensor was measured relative to temperature on the catheter balloon from 25 to 80 °C, which encompasses physiological body temperatures as well as higher temperatures that are important to consider when heating tissue for procedures like catheter ablation. From the results in Fig. 6f, the sensor provides a resistive change that is well modeled by the quadratic equation given in the figure with an $R^2$ value of 0.987.

Using the best fit quadratic equation, the average normalized percent change in resistance can be calculated for any temperature in the modeled range, which can then be used to estimate the sensitivity of the sensor. For example, the sensitivity of the sensor is calculated as $-0.42\,\frac{\%}{°C}$ in the body temperature range of 35–42 °C whereas the sensitivity for 42–80 °C is $-1.48\,\frac{\%}{°C}$. This difference in sensitivities is due to the quadratic nature of the resistive response to temperature, however, future designs will modify the graphene sensor to be most sensitive in the body temperature range in addition to reducing measured noise in the data caused by contact inconsistencies. These improvements will be achieved through optimized design tuning of the print parameters controlling graphene density in the film as well as the overall thickness while also revising the contact method for measurement to eliminate erroneous noise signals presenting in the data from the simple contact approach.

Furthermore, because the graphene sensor also exhibits a response to mechanical movement independent of temperature response, the sensor could be used for the secondary function of detecting inflation and deflation of the catheter balloon in real time as shown in Fig. 6g. When inflated, the graphene sensor on the catheter balloon is held taut in its originally printed position and shows little change from the initial resistance value. However, when the catheter balloon is deflated, the graphene sensor crumples up with the balloon surface and the sensor drops into a low-resistance state with a distinct 18% change from the initial resistive value. Drift of the resistive value for the inflated state is attributed to mechanical forces acting on the printed graphene film during the initial inflation/deflation cycles. Through collapse and expansion, the thin-film graphene eventually evolves into a more stable morphology and an approximate steady state is reached. For the graphene sensor on the catheter surface, drift of the inflated state resistive value $R_0$ was characterized in Supplementary Fig. 10, which shows that the sensor had an initial $R_0$ of ~8.9 kΩ that reached a relatively steady state value of ~10.6 kΩ after 18–20 cycles. In Fig. 5g, inflated and deflated states were detected during cycles 13–20 with a drift of ~1.5% in the inflated resistance value, which is smaller than the resistive change due to deflation and less than the

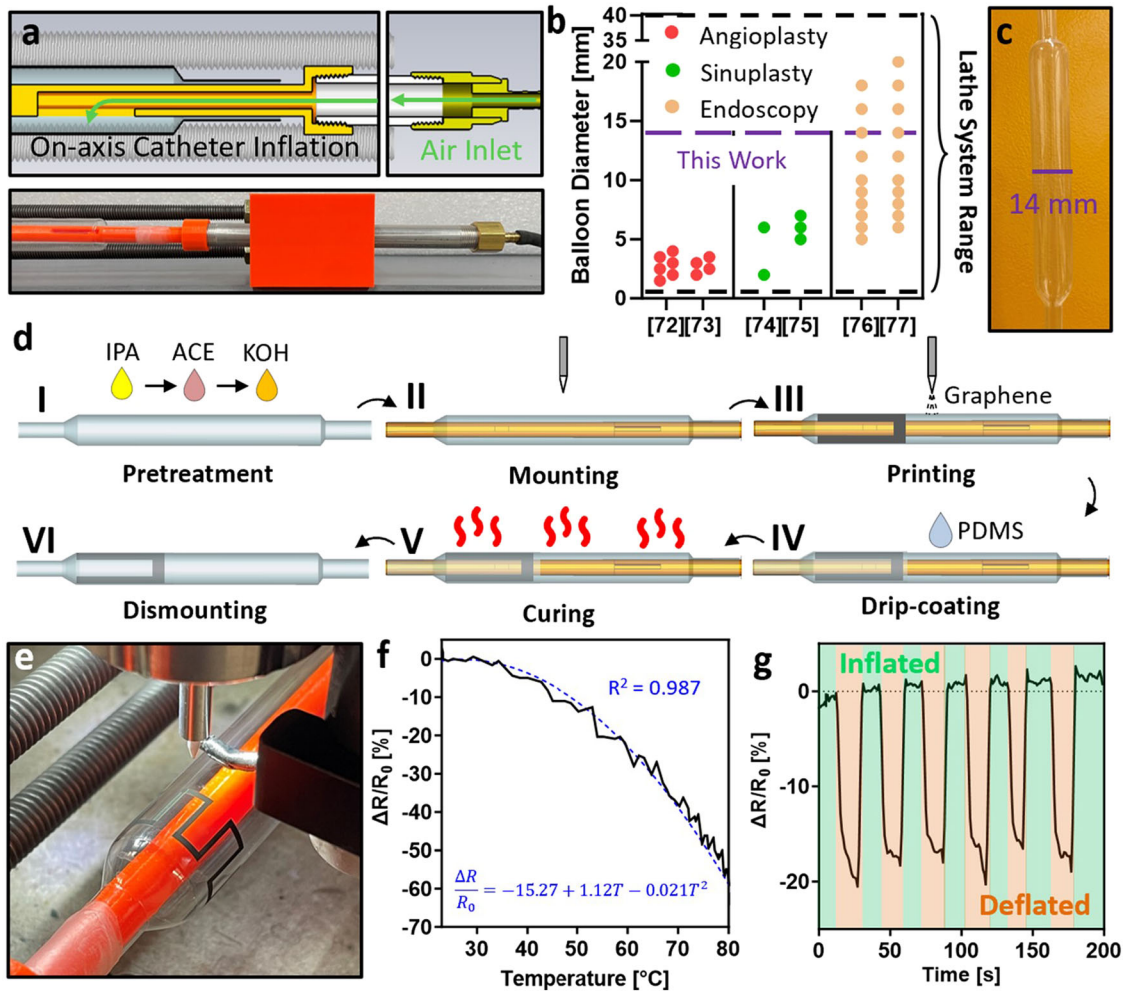


**Fig. 6 | Lathe aerosol jet printing for smart catheter functionalization. a** CAD diagram and picture of lathe mechanism showing the pathway for pumped air to achieve on-axis catheter balloon inflation. **b** Comparison plot of commercial catheter balloon diameters relative to lathe system range, which can support up to 40 mm diameter. **c** Picture of 14 mm diameter inflatable catheter balloon used for demonstration and relevant for endoscopy procedures. **d** Fabrication process for graphene sensor on catheter balloon. **e** Picture of LAJ printing graphene meander line sensor around the circumference of inflated catheter balloon. Plots of normalized resistive change of printed graphene sensor **f** versus temperature showing sensitive response and polynomial modeling with high $R^2$ fit and **g** over time as the catheter balloon is inflated and deflated illustrating the ability of the sensor to monitor inflation.

drift during the wearing-in cycles of a new sensor. With LAJ printing this sensor with two optional functionalities was trivial to fabricate directly onto the catheter balloon such that no secondary substrate or additional processing was required. The capabilities of lathe-based AJ printing coupled with the modularity of the lathe mechanism ensures that this method of DW printing can be used for virtually any catheter without requiring interaction or modification of the mechanism.

We have developed a mechanism for actively translating cartesian-coordinate motion to cylindrical-coordinate motion for use in the AM of conformal electronic devices, specifically by using AJ printing. This lathe-like mechanism in combination with AJ printing enables fully controlled and high-resolution fabrication of thin-film materials and electronic devices onto 3D rotational shapes that are difficult to accommodate without using more complex 5-axis motion systems, which are significantly expensive and difficult to scale. The most unique application of this mechanism is demonstrated by printing flexible electronic sensors directly onto an endoscopic catheter balloon. Functionalized catheters are very difficult to produce, and although there are existing AM methods that have demonstrated fabrication of catheter electronics, the lathe-based approach presented here is low-cost, efficient, and simply designed for easy scaling to commercial production demands. Additionally, given the modularity of the mechanism design, LAJ printing can be employed to produce conformal electronic devices in a number of versatile applications including for any commercially available catheter or catheter balloon.

## Methods section

### Materials

Materials used in this work for building the lathe mechanism include polyethylene terephthalate glycol (PETG) filament purchased from Prusa3D for making custom 3D-printed components, and mechanical components including rods, gears, and fasteners, which were all purchased from McMaster-Carr. Graphene ink containing exfoliated graphene flakes was purchased from Sigma-Aldrich (808261-10 ML) at a concentration of 10 wt % and diluted for printing by mixing with deionized (DI) water at a 1:2 ratio. CNCs were purchased from Cellulose Lab Inc. (CNC-Slurry-HS) with a concentration of 10 wt% in water. The CNC ink was then prepared for printing by diluting with DI water to a concentration of 6 wt% and dissolving 0.05 wt% of NaCl into the solution for optimal ionicity. The CNT ink was purchased in a toluene solution from Nanointegris (IsoSol-S100) at a concentration of 1 mg/20 mL with a 99.9% purity of semiconducting CNTs. The CNT ink was prepared for printing by diluting with additional toluene down to a concentration of 0.01 mg/mL. AgNWs with a 70 nm nanowire diameter were purchased from Sigma-Aldrich (807826-25 ML) and diluted to a 10 mg/mL concentration in DI water with 0.01 wt% of hydroxypropyl

methylcellulose mixed in to improve print quality. All inks were agitated on a vortex shaker prior to use to redisperse any settling of the inks and ensure homogeneity before printing. Flexible substrates in this work include gloss white paper used as-is, and 127 μm thick Kapton, which was treated in a 1 M potassium hydroxide (KOH) solution for 10 min to improve surface adhesion for printing. The TPU catheter balloon substrates with cylindrical body diameters of 14 mm were provided by Symple Surgical and pretreated with a 10-min KOH treatment identical to the Kapton preparation. A Sylgard 184 silicone elastomer kit with a two-part 10:1 mixture of base to curing agent was used for drip-coating PDMS onto the printed graphene sensor to serve as an encapsulation layer. A two-part silver conductive epoxy from Electron Microscopy Sciences was used to attach copper wires to the catheter-based printed graphene sensor for ease of measurement during testing.

### Aerosol jet printing process and parameters

The direct-write AM method of AJ printing used throughout this work was performed on an AJ300 printer from Optomec with a motorized planar platen and ultrasonic atomization AJ printing system. The AJ300 motorized platen and ultrasonic bath were kept at room temperature and 20 °C, respectively, across all printing, which was done with a 150 μm diameter print nozzle. The other relevant printer parameters of atomizer flow, sheath flow, ultrasonicator current, and print speed, which were used during AJ printing varied depending on the ink being atomized and jetted. These parameters are listed for each of the four inks used in this work in Supplementary Table 1.

### Lathe aerosol jet (LAJ) printing

The LAJ printing attachment was custom designed with all relevant components having been modeled using CAD in CST Microwave Studio and prepared for 3D printing by PrusaSlicer. The attachment was assembled and fastened into a single mechanism using 3D-printed parts, mechanical components, and various metal screws, which were used for joining assembled pieces and fixing the attachment to the Optomec AJ300 printer. All 3D-printed plastic (PETG) components were manufactured using an Original Prusa i3 MK3S+ fused filament deposition 3D printer. The two separate portions of the lathe attachment were fixed to the AJ300 in two locations: the upper portion of the attachment that consists of the suspended axle and positioning system was attached to an arm above the AJ300 motorized platen; and the interchangeable lower portion of the attachment, a 3D-printed housing for the rack and axle-clamp guide, was affixed to the edge of the AJ300 platen. Patterned design files for commanding the movement of the AJ300 platen into the lathe mechanism were created in AutoCAD software using cartesian coordinates and modified according to the diametric ratio. The diametric ratio that determines the translation of motion between the planar platen and the substrate-holding rotating mandrel was accounted for in all designs by multiplying the $x$-axis dimensions by the diametric ratio. The diametric ratio was ideally kept as close to 1:1 as possible for all prints with four available pinion options of 7.5, 15, 25, and 50 mm. All four pinions used the same gear module of 0.5 with the number of teeth increasing for larger diameter pinions but ensured that only one rack was needed for all testing.

Whenever LAJ printing was used with a flexible film substrate (paper or Kapton), the film would be wrapped around a 3D-printed cylinder of a chosen diameter to serve as the rotating mandrel for the substrate. After mounting the rotating mandrel and substrate on-axis, the axle position was fully leveled and normally oriented under the print nozzle using the built-in positioning rods and a bubble level. Once the upper portion of the lathe attachment was fixed in position below the nozzle, the lower portion with a pinion-specific assembly was screwed onto the end of the AJ300 platen. Then, the two portions of the lathe attachment were connected by screwing the guided axle clamp onto the end of the suspended axle with the pinion fixed in line with the rack. After these steps, the lathe mechanism was complete and the AJ300 ready to be used for lathe-based AJ printing onto curvilinear targets.

### Characterization of print morphology and trace resistance

To most easily analyze the quality of prints achieved by LAJ printing, graphene ink was used for all visualization and testing in this work due to its visibly dark and reliably dense deposition. Printed structures were imaged using optical microscopy and dimensional measurements for length, width, and pitch were obtained from these images. Whole film profile measurements were carried out using a 3D optical/laser confocal profiler (Keyence VK-X3050) with a built-in interferometer to accurately determine height. Raw data of profiles was then averaged using a rolling window of 25 data points. Film thickness was measured for the different diametric ratios using a probe tip profilometer (Bruker Dektak 150). Film resistance measurements were obtained using a source measurement unit (SMU) (Agilent B2902A) connected to a micro-probe station (Signatone H150W) with probe tip positioned at opposing ends of each measured trace. Film sheet resistance measurements were obtained using the same SMU in connection with a four-point probe assembly (Jandel Multi Height Probe) with 0.635 mm probe spacing. For all of these characterization modalities, it is only possible to measure printed structures that are flattened onto a plane, therefore, all the prints in this work (except catheter-based prints) were characterized after being removed from the cylindrical mandrel and adhered flatly onto a glass slide.

### Fabrication and characterization of LAJ printed electronic devices

To fabricate all-carbon capacitors with LAJ printing, a paper substrate was wrapped around a 15 mm diameter cylinder, which served as the rotating mandrel. An initial layer of graphene was used to pattern the 1.5 × 2.6 mm bottom electrodes of the capacitors followed by a single pass for the dielectric CNC layer, and a third layer of graphene for top electrodes of 0.45 × 1.88 mm. The parallel-plate capacitors were then measured with probes and a semiconductor device analyzer (Agilent B1500), which was able to obtain capacitive measurements across frequency from 1 kHz to 1 MHz. Then, using the same probe setup but attached to the SMU, charging/discharging characteristics of the capacitors were measured with voltages from 0.5 to 2 V.

To fabricate all-carbon TFTs, a paper substrate was wrapped around a 25 mm diameter cylindrical mandrel, and graphene was printed to form source/drain contacts and fiducial marks in opposing corners for alignment. These crosshair fiducial marks provide a focusing point to correctly align the nozzle height above the substrate and to adjust for any lateral misalignment in the $\hat{z}$ or $\hat{\theta}$ directions on the mandrel with an alignment accuracy of ±5 μm as determined by the system movement and the alignment camera used for focusing. Then, by using the fiducial marks to align subsequent layers, CNTs were printed to form a 225 μm long by 200 μm wide channel followed by a CNC dielectric layer and finished off by a graphene top-gate contact. These TFT devices were then tested by probing 1 $mm^2$ contact pads at the source, drain, and gate and using an SMU to obtain full characteristics with a source to drain voltage of −0.5 V and a gate voltage swept from −1 to 1 V at a sweep rate of 20 mV/s.

### LAJ printing with complex substrates

For the complex substrate LAJ printing demonstrations, the lathe mechanism was used identically to how it was described previously except a diametric ratio of 1:1 was only possible for the 15 mm concave substrate. Therefore, when printing onto the PETG cone and the 1000 μL pipette tip, the 15 mm pinion was used because it was closest to the largest diameter of each substrate and thus allowed for less extreme diametric ratios. In the concave substrate case, the only modification to the print setup was to remove the nozzle shutter, which is normally used to block the jetted material and provide cleaner patterning. A graphene meander line with 1 mm trace widths was patterned directly onto the concave PETG surface. Then, graphene pads with connecting traces were deposited onto a concavely situated paper substrate. For the PETG cone, two passes of AgNWs were printed using the previously reported printer parameters. For the pipette tip, five separate lines of printed

graphene were printed around the circumference of the pipette tip and connected end to end to form a continuous helical trace starting from the 1 mm diameter end of the tip.

### Catheter-based graphene sensor fabrication and testing

Beginning with a KOH-treated catheter balloon, the balloon was threaded onto a hollow 3D-printed PETG axle and then mounted onto the lathe mechanism with a freely rotating inflation port. The inflation port was connected by tubing to an external pressure pump that was used to keep the catheter balloon under constant inflation throughout the print process. While inflated, a 7-turn graphene meander line with trace width of 1 and 6 mm spacing between turns was printed onto the cylindrical body of the catheter balloon with pads at each end for electrical connection. Silver epoxy was used to attach copper wire leads onto these graphene pads and allowed 1 h to cure for a rigid connection. Then, the entire sensor and epoxied pads were drip-coated with the Sylgard 184 PDMS mixture. After coating, the sample balloon was placed into an oven at 65 °C for 1.5 h to promote rapid curing of the PDMS encapsulation layer without using a temperature that would cause degradation of the TPU catheter balloon. Alternatively, a longer room-temperature cure could also be used at this step to avoid heating entirely.

To test the graphene sensor functionality, alligator clips were attached to the epoxied copper wires and the resistance of the meander line was measured by an SMU and recorded over time. To gauge the change in resistance relative to a change in temperature, a MAX31855 Type-K thermocouple and Adafruit Feather M0 Bluefruit microcontroller were used to measure the temperature on the catheter balloon surface adjacent to the printed meander line. The temperature from the thermocouple was measured in tandem with the resistance of the graphene meander line and timestamped for each moment a measurement was taken. This method provided a resistive value for each relative temperature as the device was tested by applying hot air over the catheter balloon using a heat gun set to 400 °C. The device was tested in an inflated state, as it would be when used in a medical setting within the body, and the change in temperature versus change in resistance of the printed meander line was observed. Then, using the same testing setup the resistance of the meander line was measured with respect to time as the pressure pump was turned off and on to allow the catheter balloon to enter deflated and inflated states, respectively.

## Data availability

The data that supports the plotted results and findings of this study are available from the corresponding author upon reasonable request.

Received: 21 May 2024; Accepted: 12 August 2024;
Published online: 30 August 2024

## References

1. Chua, C. K., Yeong, W. Y., Low, H. Y., Tran, T. & Tan, H. W. *3D Printing and Additive Manufacturing of Electronics: Principles and Applications* (World Scientific, 2021).
2. Lu, B.-H., Lan, H.-B. & Liu, H.-Z. Additive manufacturing frontier: 3D printing electronics. *Opto-Electron. Adv.* **1**, 17000401–17000410 (2018).
3. Tan, H. W., Choong, Y. Y. C., Kuo, C. N., Low, H. Y. & Chua, C. K. 3D printed electronics: processes, materials and future trends. *Prog. Mater. Sci.* **127**, 100945 (2022).
4. Ahn, C. H. & Allen, M. G. Micromachined planar inductors on silicon wafers for MEMS applications. In *IEEE Transactions on Industrial Electronics* Vol. 45, 866–876 (IEEE, 1998).
5. Streppel, U. et al. New wafer-scale fabrication method for stacked optical waveguide interconnects and 3D micro-optic structures using photoresponsive (inorganic–organic hybrid) polymers. *Opt. Mater.* **21**, 475–483 (2003).
6. Saengchairat, N., Tran, T. & Chua, C.-K. A review: additive manufacturing for active electronic components. *Virtual Phys. Prototyp.* **12**, 31–46 (2016).
7. Huang, Z., Shao, G. & Li, L. Micro/nano functional devices fabricated by additive manufacturing. *Prog. Mater. Sci.* **131**, 101020 (2023).
8. Corzo, D., Tostado-Blázquez, G. & Baran, D. Flexible Electronics: Status, Challenges and Opportunities. *Front. Electron.* **1**, 594003 (2020).
9. Koo, J. H., Kim, D. C., Shim, H. J., Kim, T. H. & Kim, D. H. Flexible and stretchable smart display: materials, fabrication, device design, and system integration. *Adv. Funct. Mater.* **28**, 1801834 (2018).
10. Rogers, J. A., Someya, T. & Huang, Y. Materials and mechanics for stretchable electronics. *Science* **327**, 1603–1607 (2010).
11. Falco, A., Petrelli, M., Bezzeccheri, E., Abdelhalim, A. & Lugli, P. Towards 3D-printed organic electronics: planarization and spray-deposition of functional layers onto 3D-printed objects. *Org. Electron.* **39**, 340–347 (2016).
12. Dimitrakopoulos, C. D. & Malenfant, P. R. L. Organic thin film transistors for large area electronics. *Adv. Mater.* **14**, 99–117 (2002).
13. Hyun, W. J. et al. All-printed, foldable organic thin-film transistors on glassine paper. *Adv. Mater.* **27**, 7058–7064 (2015).
14. Huang, Y. et al. Assembly and applications of 3D conformal electronics on curvilinear surfaces. *Mater. Horiz.* **6**, 642–683 (2019).
15. Wu, H. et al. Fabrication techniques for curved electronics on arbitrary surfaces. *Adv. Mater. Technol.* **5**, 2000093 (2020).
16. Ershad, F. et al. Ultra-conformal drawn-on-skin electronics for multifunctional motion artifact-free sensing and point-of-care treatment. *Nat. Commun.* **11**, 3823 (2020).
17. Kim, H. et al. Fully integrated, stretchable, wireless skin-conformal bioelectronics for continuous stress monitoring in daily life. *Adv. Sci.* **7**, 2000810 (2020).
18. Li, H. et al. Breathable and skin-conformal electronics with hybrid integration of microfabricated multifunctional sensors and kirigami-structured nanofibrous substrates. *Adv. Funct. Mater.* **32**, 2202792 (2022).
19. Liu, Y., Pharr, M. & Salvatore, G. A. Lab-on-skin: a review of flexible and stretchable electronics for wearable health monitoring. *ACS Nano* **11**, 9614–9635 (2017).
20. Beziuk, G., Baum, T. C., Ghorbani, K. & Nicholson, K. J. Structurally integrated radar in an aerospace composite laminate. *IEEE Trans. Compon. Packag. Manuf. Technol.* **11**, 1835–1843 (2021).
21. Feng, Y., Yazawa, K. & Lu, N. High-performance conformal thermoelectric generator for environmental monitoring. *ACS Appl. Electron. Mater.* **4**, 197–205 (2022).
22. Collado, A. & Georgiadis, A. Conformal hybrid solar and electromagnetic (EM) energy harvesting rectenna. In *IEEE Transactions on Circuits and Systems I: Regular Papers* Vol. 60, 2225–2234 (IEEE, 2013).
23. Yazawa, K., Feng, Y. & Lu, N. Conformal heat energy harvester on Steam4 pipelines for powering IoT sensors. *Energy Convers Manag* **244** (2021).
24. Chang, J.-H. et al. Direct imprinting using soft mold and gas pressure for large area and curved surfaces. *J. Vac. Sci. Technol. A Vac. Surf. Films* **23**, 1687–1690 (2005).
25. Sim, K. et al. Three-dimensional curvy electronics created using conformal additive stamp printing. *Nat. Electron.* **2**, 471–479 (2019).
26. Le Borgne, B., De Sagazan, O., Crand, S., Jacques, E. & Harnois, M. Conformal electronics wrapped around daily life objects using an original method: water transfer printing. *ACS Appl. Mater. Interfaces* **9**, 29424–29429 (2017).
27. Zhang, S. et al. High-fidelity conformal printing of 3D liquid alloy circuits for soft electronics. *ACS Appl Mater. Interfaces* **11**, 7148–7156 (2019).
28. Alkadi, F., Lee, K. C., Bashiri, A. H. & Choi, J. W. Conformal additive manufacturing using a direct-print process. *Addit. Manuf.* **32**, 100975 (2020).

29. Biasetto, L. et al. Direct ink writing of cylindrical lattice structures: a proof of concept. *Open Ceram.* **7**, 100139 (2021).
30. Vatani, M., Engeberg, E. D. & Choi, J.-W. Conformal direct-print of piezoresistive polymer/nanocomposites for compliant multi-layer tactile sensors. *Addit. Manuf.* **7**, 73–82 (2015).
31. Zhang, Y., Liu, C. Q. & Whalley, D. Direct-write techniques for maskless production of microelectronics: a review of current state-of-the-art technologies. In *2009 International Conference on Electronic Packaging Technology & High Density Packaging (Icept-Hdp 2009)* 421–427 (IEEE, 2009).
32. Christenson, K. K., Paulsen, J. A., Renn, M. J., McDonald, K. & Bourassa, J. Direct printing of circuit boards using Aerosol Jet®. *NIP Digit. Fabr. Conf.* **27**, 433–436 (2011).
33. Gupta, A. A., Bolduc, A., Cloutier, S. G. & Izquierdo, R. Aerosol jet printing for printed electronics rapid prototyping. In *IEEE International Symposium on Circuits and Systems* 866–869 (IEEEE, 2016).
34. Valayil Varghese, T. et al. Multijet gold nanoparticle inks for additive manufacturing of printed and wearable electronics. *ACS Mater. Au* **4**, 65–73 (2024).
35. Singh, M., Haverinen, H. M., Dhagat, P. & Jabbour, G. E. Inkjet printing-process and its applications. *Adv. Mater.* **22**, 673–685 (2010).
36. Secor, E. B., Prabhumirashi, P. L., Puntambekar, K., Geier, M. L. & Hersam, M. C. Inkjet printing of high conductivity, flexible graphene patterns. *J. Phys. Chem. Lett.* **4**, 1347–1351 (2013).
37. Hondred, J. A., Stromberg, L. R., Mosher, C. L. & Claussen, J. C. High-resolution graphene films for electrochemical sensing via inkjet maskless lithography. *ACS Nano* **11**, 9836–9845 (2017).
38. Giannakou, P., Tas, M. O., Le Borgne, B. & Shkunov, M. Water-transferred, inkjet-printed supercapacitors toward conformal and epidermal energy storage. *ACS Appl. Mater. Interfaces* **12**, 8456–8465 (2020).
39. Yan, K., Li, J., Pan, L. & Shi, Y. Inkjet printing for flexible and wearable electronics. *APL Mater*. **8**, 120705 (2020).
40. Paulsen, J. A., Renn, M., Christenson, K., & Plourde, R. Printing conformal electronics on 3D structures with Aerosol Jet technology. In *Proc. 2012 Future of Instrumentation International Workshop (FIIW) Proceedings* 1–4 (IEEE, 2012).
41. Williams, N. X. et al. Silver nanowire inks for direct-write electronic tattoo applications. *Nanoscale* **11**, 14294–14302 (2019).
42. Secor, E. B. Principles of aerosol jet printing. *Flex. Print. Electron.* **3**, 035002 (2018).
43. Rurup, J. D. & Secor, E. B. Understanding oblique deposition in aerosol jet printing for conformal electronics fabrication. *J. Manuf. Process.* **120**, 1231–1240 (2024).
44. Vella, S., Smithson, C., Halfyard, K., Shen, E. & Chrétien, M. Integrated capacitive sensor devices aerosol jet printed on 3D objects. *Flex. Print. Electron.* **4**, 045005 (2019).
45. Gu, Y. et al. Direct-write printed broadband inductors. *Addit. Manuf.* **30**, 100843 (2019).
46. Goh, G. L. et al. Fabrication of design-optimized multifunctional safety cage with conformal circuits for drone using hybrid 3D printing technology. *Int. J. Adv. Manuf. Technol.* **120**, 2573–2586 (2022).
47. Gu, Y., Park, D., Bowen, D., Das, S. & Hines, D. R. Direct-write printed, solid-core solenoid inductors with commercially relevant inductances. *Adv. Mater. Technol.* **4**, 1800312 (2018).
48. Hong, F., Lampret, B., Myant, C., Hodges, S. & Boyle, D. 5-axis multi-material 3D printing of curved electrical traces. *Addit. Manuf.* **70**, 103546 (2023).
49. Lamport, E., Luce, A., Piro, Y., Trulli, S. & Akyurtlu, A. *Proc. 2023 IEEE 73rd Electronic Components and Technology Conference (ECTC)* 2207–2212 (IEEE, 2023).
50. Adler, S. N., Bjarnason, I. & Metzger, Y. C. New balloon-guided technique for deep small-intestine endoscopy using standard endoscopes. *Endoscopy* **40**, 502–505 (2008).
51. Byrne, R. A., Stone, G. W., Ormiston, J. & Kastrati, A. Coronary balloon angioplasty, stents, and scaffolds. *Lancet* **390**, 781–792 (2017).
52. Bukka, M., Rednam, P. J. & Sinha, M. Drug-eluting balloon: design, technology and clinical aspects. *Biomed. Mater.* **13**, 032001 (2018).
53. Su, Y. et al. Mechanics of stretchable electronics on balloon catheter under extreme deformation. *Int. J. Solids Struct.* **51**, 1555–1561 (2014).
54. Han, M. et al. Catheter-integrated soft multilayer electronic arrays for multiplexed sensing and actuation during cardiac surgery. *Nat. Biomed. Eng.* **4**, 997–1009 (2020).
55. Lee, S. P. et al. Catheter-based systems with integrated stretchable sensors and conductors in cardiac electrophysiology. In *Proc. IEEE* Vol. 103, 682–689 (IEEE, 2015).
56. Wang, D., Dong, R., Wang, X. & Jiang, X. Flexible electronic catheter based on nanofibers for the in vivo elimination of circulating tumor cells. *ACS Nano* **16**, 5274–5283 (2022).
57. Yan, Z. et al. Thermal release transfer printing for stretchable conformal bioelectronics. *Adv. Sci.* **4**, 1700251 (2017).
58. Klinker, L. et al. Balloon catheters with integrated stretchable electronics for electrical stimulation, ablation and blood flow monitoring. *Extreme Mech. Lett.* **3**, 45–54 (2015).
59. Rivkin, B. et al. Electronically integrated microcatheters based on self-assembling polymer films. *Sci. Adv.* **7**, eabl5408 (2021).
60. Sharma, T., Aroom, K., Naik, S., Gill, B. & Zhang, J. X. Flexible thin-film PVDF-TrFE based pressure sensor for smart catheter applications. *Ann. Biomed. Eng.* **41**, 744–751 (2013).
61. Jordan, C. D. et al. Wireless resonant circuits printed using aerosol jet deposition for MRI catheter tracking. In *IEEE Transactions on Biomedical Engineering* Vol. 67, 876–882 (IEEE, 2020).
62. Will, K. et al. Pre-tuned resonant marker for iMRI using aerosol deposition on polymer catheters. In *Proc. SPIE* Vol. 7625 (SPIE, 2010).
63. Annapragada, S. R., Murthy, J. Y. & Garimella, S. V. Prediction of droplet dynamics on an incline. *Int. J. Heat. Mass Tranf.* **55**, 1466–1474 (2012).
64. Yilbas, B. S., Al-Sharafi, A., Ali, H. & Al-Aqeeli, N. Dynamics of a water droplet on a hydrophobic inclined surface: influence of droplet size and surface inclination angle on droplet rolling. *RSC Adv.* **7**, 48806–48818 (2017).
65. Salary, R., Lombardi, J. P., Weerawarne, D. L., Rao, P. & Poliks, M. D. A computational fluid dynamics investigation of pneumatic atomization, aerosol transport, and deposition in aerosol jet printing process. *J. Micro Nano Manuf.* **9**, 010903 (2021).
66. Williams, N. X., Bullard, G., Brooke, N., Therien, M. J. & Franklin, A. D. Printable and recyclable carbon electronics using crystalline nanocellulose dielectrics. *Nat. Electron.* **4**, 261–268 (2021).
67. Smith, B. N. et al. Ionic dielectrics for fully printed carbon nanotube transistors: impact of composition and induced stresses. *Nanoscale* **14**, 16845–16856 (2022).
68. Franklin, E. G., Smith, B. & Franklin, A. D. Impact of NaCl concentration in crystalline nanocellulose for printed ionic dielectrics. *J. Emerg. Investig.* (2023).
69. Lu, S., Smith, B. N., Meikle, H., Therien, M. J. & Franklin, A. D. All-carbon thin-film transistors using water-only printing. *Nano Lett.* **23**, 2100–2106 (2023).
70. Herbert, R., Lim, H. R., Rigo, B. & Yeo, W. H. Fully implantable wireless batteryless vascular electronics with printed soft sensors for multiplex sensing of hemodynamics. *Sci. Adv.* **8**, eabm1175 (2022).
71. Rigo, B. et al. Soft implantable printed bioelectronic system for wireless continuous monitoring of restenosis. *Biosens. Bioelectron.* **241**, 115650 (2023).
72. Boston Scientific Coyote™ and Coyote™ ES. https://www.bostonscientific.com/en-US/products/catheters--balloon/coyote-balloon-dilatation-catheter.html (2024).

73. Philips AngioSculpt Evo. https://www.usa.philips.com/healthcare/product/HCIGTDASEVOBC/angiosculpt-evo-scoring-balloon-catheter#documents (2024).
74. Acclarent RELIEVA SPINPLUS® Balloon Sinuplasty System. https://www.jnjmedtech.com/en-US/acclarent-integra/product/relieva-spinplus-balloon-sinuplasty-system (2023).
75. Meril MESIRE™ Balloon Sinus Dilation System. https://www.merillife.com/assets/pdfs/medical-devices/mesire-1632217477pdf.pdf (2024).
76. Olympus EZDilate™ Endoscopic Balloon Dilator. https://medical.olympusamerica.com/products/ezdilate-endoscopic-balloon-dilator (2024)
77. Boston Scientific CRE™ Balloon Dilatation Catheters. https://www.bostonscientific.com/en-US/products/Balloons-Dilation-Extraction/cre-wireguided-balloon-dilation.html (2024).
78. Kochhar, R. et al. Endoscopic balloon dilatation is an effective management strategy for caustic-induced gastric outlet obstruction: a 15-year single center experience. *Endosc. Int. Open* **7**, E53–E61 (2019).
79. Tung, T. T. et al. Recent advances in sensing applications of graphene assemblies and their composites. *Adv. Funct. Mater.* **27**, 1702891 (2017).


## Acknowledgements

This work was supported in part by funding from the National Institutes of Health (NIH) under award nos. 1R01HL146849, 1R43CA257701-01A1 (Symple Surgical), and 1R43HD112219-01A1 (H3Pelvic Therapy Systems). This work was performed in part at the Duke University Shared Materials Instrumentation Facility (SMIF), a member of the North Carolina Research Triangle Nanotechnology Network (RTNN), which is supported by the National Science Foundation (grant no. ECCS-1542015) as part of the National Nanotechnology Coordinated Infrastructure (NNCI). We would like to thank Sohail Desai of Symple Surgical and Zachary Lyon of H3Pelvic Therapy Systems for their support of this research. We also gratefully acknowledge CST Microwave Studio, Ansys, and Keysight for providing discounted software for this research.

## Author contributions

H.A.H., P.M., and A.D.F. conceived the relevant ideas for this project. H.A.H. developed the lathe mechanism, designed the experiments, and conducted all printing. J.L.D. contributed to the manufacture of 3D printed and metal components used in the lathe mechanism. B.N.S. prepared inks and aided in device design. P.M. advised on mechanism development and process integration for catheter balloons. H.A.H. and A.D.F. analyzed the data and wrote the manuscript. All authors have read the manuscript, were involved in modifications, and approved of the final manuscript.

## Competing interests

The authors declare no competing interests.

## Additional information

**Supplementary information** The online version contains supplementary material available at https://doi.org/10.1038/s41528-024-00340-0.

**Correspondence** and requests for materials should be addressed to Aaron D. Franklin.